Title

Hypoxia-Responsive Stereocomplex Polymeric Micelles with Improved Drug Loading Inhibit Breast Cancer Metastasis in an Orthotopic Murine Model

Journal

ACS Applied Materials & Interfaces, 14(18)

ISSN

1944-8244

Authors

Lu, Min

Huang, Xu

Cai, Xiaohui

et al.

Publication Date

2022-05-11

DOI

10.1021/acsami.1c23737

ACS APPLIED MATERIALS & INTERFACES

www.acsami.org

Research Article

Hypoxia-Responsive Stereocomplex Polymeric Micelles with Improved Drug Loading Inhibit Breast Cancer Metastasis in an Orthotopic Murine Model

Min Lu,[§] Xu Huang,[§] Xiaohui Cai, Jiajia Sun, Xuemeng Liu, Lingyan Weng, Li Zhu,* Qianqian Luo,* and Zhongping Chen*

Cite This: *ACS Appl. Mater. Interfaces* 2022, 14, 20551−20565

Read Online

ACCESS | Metrics & More | Article Recommendations | Supporting Information

ABSTRACT: Tumor metastasis is a leading cause of breast cancer-related death. Taxane-loaded polymeric formulations, such as Genexol PM and Nanoxel M using poly(ethylene glycol)-poly(D,L-lactide) (PEG-PLA) micelles as drug carriers, have been approved for the treatment of metastatic breast cancer. Unfortunately, the physical instability of PEG-PLA micelles, leading to poor drug loading, premature drug leakage, and consequently limited drug delivery to tumors, largely hinders their therapeutic outcome. Inspired by the enantiomeric nature of PLA, this work developed stereocomplex PEG-PLA micelles through stereoselective interactions of enantiomeric PLA, which are further incorporated with a hypoxia-responsive moiety used as a hypoxia-cleavable linker of PEG and PLA, to maximize therapeutic outcomes. The results showed that the obtained micelles had high structural stability, showing improved drug loading for effective drug delivery to tumors as well as other tissues. Especially, they were capable of sensitively responding to the hypoxic tumor environment for drug release, reversing hypoxia-induced drug resistance and hypoxia-promoted cell migration for enhanced bioavailability under hypoxia. *In vivo* results further showed that the micelles, especially at a high dose, inhibited the growth of the primary tumor and improved tumor pathological conditions, consequently remarkably inhibiting its metastasis to the lungs and liver, while not causing any systemic toxicity. Hypoxia-responsive stereocomplex micelles thus emerge as a reliable drug delivery system to treat breast cancer metastasis.

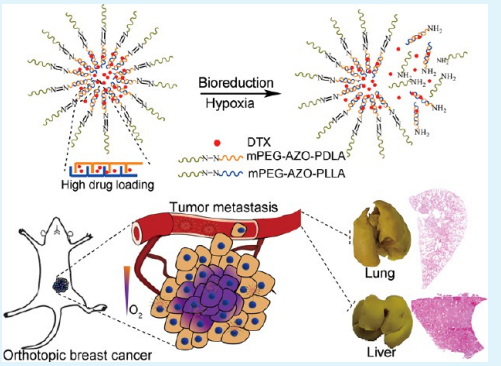

KEYWORDS: *polymeric micelles, stereocomplex, hypoxia-responsiveness, drug delivery, breast cancer, tumor metastasis*

INTRODUCTION

Breast cancer is one of the most common cancer types that affect women, accounting for 30% of newly diagnosed cases globally, and remains the second leading cause of cancer-related death after lung cancer in women.[1] Localized breast cancer generally has a high 5 year survival rate, up to 90% in developed countries.[2] Once metastasized to distant organs, such as the lungs, liver, and brain, it becomes largely incurable with its 5 year survival rate sharply decreasing to approximately 20%, leading to 90% of breast cancer-caused death.[3] Chemotherapy is one of the standard treatment regimens to treat locally advanced and metastatic breast cancer. Currently, taxanes including paclitaxel (PTX) and docetaxel (DTX), the first-generation taxanes, and cabazitaxel (CTX), the second-generation taxane, are the most effective and widely used therapeutic agents in treating both advanced and metastatic breast cancer. However, taxanes are poorly water-soluble, and the use of nonionic surfactants, such as Cremophor EL and Tween 80, as solubilization agents, is required, which leads to severe side effects. This triggers the development of new surfactant-free taxane formulations.

Biocompatible and biodegradable polymers have been extensively studied as pharmaceutical excipients, due to their diversity and flexibility in the structure and physicochemical properties. With the development of nanotechnology, polymers are designed as nanoparticle-based drug carriers to carry drugs, improve their pharmacokinetic profile, and deliver them to target sites. In comparison to other polymer-based nanoparticles, such as polymersomes and hydrogels, polymeric micelles self-assembled from amphiphilic block copolymers in an aqueous solution have a high percentage of the hydrophobic core and are very suitable for carrying taxanes.[4] Moreover, as most antitumor drugs in clinics are hydrophobic, polymeric micelles are thus a particularly valuable system for cancer indications. Poly(ethylene glycol) and poly(D,L-lactide) (PLA)

Received: December 8, 2021
Accepted: April 19, 2022
Published: April 27, 2022

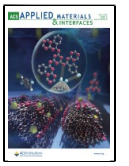

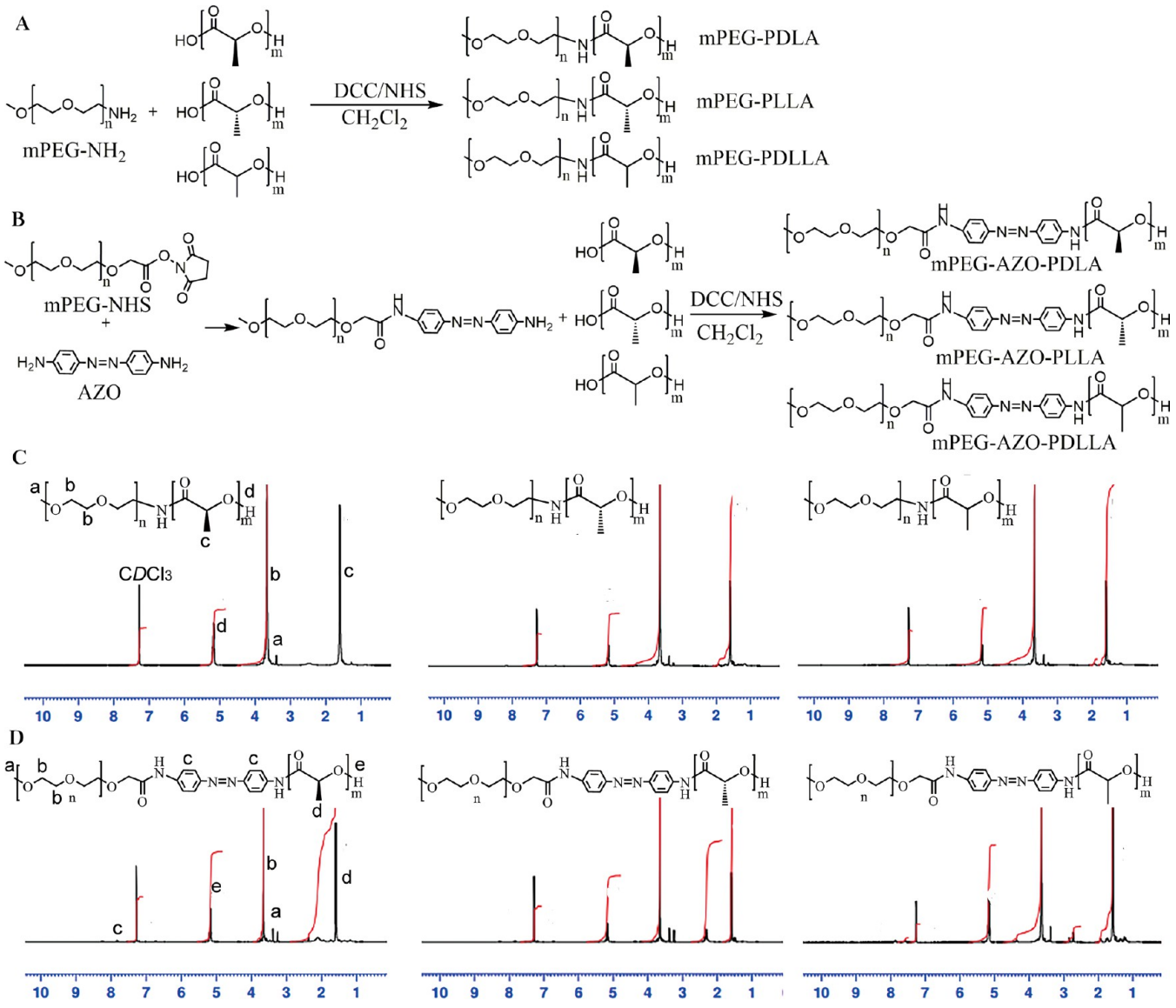

Figure 1. Synthesis and characterization of the copolymers. Synthetic procedures for (A) mPEG-PDLA, mPEG-PLLA, and mPEG-PLA and (B) mPEG-AZO-PDLA, mPEG-AZO-PLLA, and mPEG-AZO-PLA. ^{1}H NMR spectra of (C) mPEG-PDLA, mPEG-PLLA, and mPEG-PLA and (D) mPEG-AZO-PDLA, mPEG-AZO-PLLA, and mPEG-AZO-PLA.

are approved polymers for human use and their block copolymer (PEG-PLA) is the most commercially successful material for drug delivery.[5] Two PLA-PEG polymeric micelle formulations, Genexol PM and Nanoxel M carrying PTX and DTX, respectively, have been approved to treat multiple types of cancer. Clinical data evidenced that Genexol PM and Nanoxel M generally had a high maximum tolerated dose (MTD), low systemic toxicity, and at least an equal therapeutic outcome in comparison to their conventional formulations.[6,7] Despite great successes, one major obstacle of PEG-PLA micelles that limits their application is instability. For example, Nanoxel M was found to remain stable for only up to 6 h after reconstitution with saline for injection;[8] Genexol PM released 95% of loaded PTX under sink conditions within 48 h.[9] This issue leads to premature drug release, which not only increases the risk of high drug exposure to healthy tissues but also limits drug delivery to tumor sites. Tremendous efforts have been exerted to improve the stability of polymeric micelles by exploiting chemical cross-linking of either core or shell segments or noncovalent interactions between copolymers, such as hydrophobic, electrostatic, host−guest, hydrogen bonding, coordination, and stereocomplex interactions.[10] Among them, stereocomplexation through stereoselective interactions between two enantiomeric polymers, resulting in significant improvements in thermal and mechanical performances compared with parent polymers, has gained increasing attention. Enantiomeric poly(ethylene glycol)-poly(D-lactide) (PEG-PDLA) and poly(ethylene glycol)-poly(L-lactide) (PEG-PLLA) are the most studied copolymers for stereocomplexation.[11] Various stereocomplex PEG-PLA polymeric micelles based on stereocomplexation between PLA[12,13] or between PLA and PLA-conjugated prodrug[14−17] have been designed. High drug-loading capacity (DLC) and high stability after drug loading are reported in these cases.

Apart from possessing high stability when circulating in blood, an ideal drug delivery system should be capable of releasing its payloads quickly once reaching tumor sites. High stability of a carrier implies slow drug release even at tumor

https://doi.org/10.1021/acsami.1c23737
ACS Appl. Mater. Interfaces 2022, 14, 20551−20565

sites, resulting in local drug concentrations remaining low, not enough to kill tumor cells. We previously reported a silane-containing hybrid liposomal system, and *in vivo* results revealed that drug-loaded hybrid micelles with improved stability against undesirable drug leakage even had a limited therapeutic outcome, as compared to free drugs.[18] In this context, stereocomplexation is, in part, unfavorable to the ultimate therapeutic outcome of the micelles. Endowing stereocomplex polymeric micelles with a stimuli-responsive property that causes micelle destabilization for on-demand drug release is a potential modality to solve this problem.

Stimuli-responsive polymeric micelles that can respond to acidic pH, overexpressed specific enzymes, high redox potential, and hypoxia from tumor microenvironments have been extensively explored for controllable drug release.[19−22] According to our previous findings, a hypoxia-responsive drug delivery system, showing high sensitivity in responding to hypoxia and universal applicability regardless of tumor cell types, is a more reliable system.[18,23−25] Considering this, we herein designed DTX-loaded stereocomplex PEG-PLA micelles incorporated with a hypoxia-responsive moiety to maximize therapeutic outcomes and minimize undesirable side effects in treating breast cancer metastasis. The obtained micelles showed a high drug-loading capacity and a high stability after drug loading, as compared to enantiomeric and racemic micelles. More importantly, they could sensitively respond to hypoxia *in vitro* and *in vivo* for accelerated drug release. Due to the successful drug delivery and enhanced bioavailability under hypoxia, the micelles were capable of effectively inhibiting breast cancer growth and its metastasis to the lungs and liver.

2. MATERIALS AND METHODS

2.1. Materials. Enantiomeric PDLA and PLLA (M_w = 2000), racemic PLA (M_w = 2000), methylated PEG with an amino-terminal (mPEG-NH_2, M_w = 2000), and *N*-hydroxysuccinimide-terminated mPEG (mPEG-NHS, M_w = 2000) were purchased from Tuoyang (Shanghai, China). Rhodamine B (RhB), dicyclohexylcarbodiimide (DCC), *N*-hydroxysuccinimide (NHS), sodium hydrosulfite (NaS_2O_4), azobenzene-4,4-diamino (AZO), and docetaxel (DTX) were obtained from J&K Scientific Ltd. (Beijing, China). The near-infrared-emitting (NIR) fluorescent dye Cy5.5 was purchased from Lumiprobe Corporation (FL). All other chemicals were from Sinopharm Chemical Reagent Co., Ltd. (Shanghai, China). All reagents were of analytical grade and used as received. Millipore water was used for all experiments unless otherwise noted.

The human triple-negative breast cancer cell line (MDA-MB-231) and mouse breast cancer cell line (4T-1) were got from the Institute of Biochemistry and Cell Biology (Shanghai, China). Hoechst 33342 (Hoechst), 3-(4,5-dimethylthiazol-2-yl)-2,5-diphenyltetrazolium bromide (MTT), and a calcein-AM/propidium iodide (PI) double stain kit were purchased from Beyotime (Shanghai, China). BALB/c mice (6 weeks, 15−20 g, female) were supplied by the Animal Center of Nantong University and used under the guidance of the Animal Care and Use Committee of Nantong University.

2.2. Synthetic Procedures. *2.2.1. Synthesis of Copolymers.* Nonresponsive mPEG-PDLA, mPEG-PLLA, and mPEG-PLA were synthesized through the classic amide reaction of PEG-NH_2 with PLA having a carboxyl terminal in the presence of DCC and NHS. Hypoxia-responsive copolymers were synthesized via two steps: (1) synthesis of mPEG-AZO through activated mPEG-NHS and AZO and (2) synthesis of mPEG-AZO-PDLA, mPEG-AZO-PLLA, and mPEG-AZO-PLA through the amide reaction of PEG-AZO with PDLA, PLLA, and PLA, respectively. Detailed synthetic procedures are shown in Figure 1 and the Supporting Information. The structure of the obtained copolymers was verified by ^{1}H NMR on a 400 MHz NMR spectrometer (Avance III, Bruker) using $CDCl_3$ as the solvent.

2.2.2. Preparation of Polymeric Micelles. Polymeric micelles were prepared through the self-assembly technique. In a typical experiment to synthesize hypoxia-responsive stereocomplex micelles (AZO-SC-PMs), 10 mg of mPEG-AZO-PDLA and 10 mg of mPEG-AZO-PLLA were dissolved in 2 mL of dimethyl sulfoxide (DMSO), followed by the addition of 10 mL of water drop by drop with vigorous stirring. The mixture was then dialyzed against water for 24 h to obtain AZO-SC-PMs. Hypoxia-responsive enantiomeric polymeric micelles (AZO-D-PMs and AZO-L-PMs) and racemic polymeric micelles (AZO-DL-PMs) as well as nonresponsive D-PMs, L-PMs, DL-PMs, and SC-PMs were also prepared using their corresponding copolymers. The critical micelle concentration (CMC) of micelles in water was determined by the dynamic light scattering technique (DLS, Zetasizer ZS90, Malvern) proposed by previous work.[26,27] The intersection of regression lines from the plot of scattering intensity against the copolymer concentration was calculated as CMC.

Drug-loaded polymeric micelles (D-PMs/DTX, L-PMs/DTX, DL-PMs/DTX, SC-PMs/DTX, AZO-D-PMs/DTX, AZO-L-PMs/DTX, AZO-DL-PMs/DTX, and AZO-SC-PMs/DTX) were prepared by dissolving DTX with the copolymers in DMSO based on the procedure described above. Similarly, RhB and Cy5.5-labeled polymeric micelles were also prepared for *in vitro* and *in vivo* fluorescence observation, respectively.

2.3. Micelle Characterization. *2.3.1. Size, Morphology, and Surface Properties.* The size and morphology of micelles were observed on a transmission electron microscope (TEM, JEM-1230, Japan) operating at 80.0 kV, and their hydrodynamic size, polydispersity index (PDI), and surface properties were determined by DLS. Samples were dropped on a copper grid and dispersed in water for TEM and DLS characterization, respectively.

2.3.2. Stereocomplexation. X-ray diffraction (XRD) measurements were carried out to verify stereocomplexation on a diffractometer operating under 40 kV voltage and 40 mA current using Cu Kα radiation (λ = 0.15418 nm) (D8 Advance, Bruker). Thermal properties of the stereocomplex structure were studied by differential scanning calorimetry (DSC) and thermogravimetric analysis (TGA) (STA 449 F5, Netzsch) in a N_2 environment at a heating rate of 20 °C/min.

2.3.3. Drug Loading. Drug-loading efficiency (DLE, %) and drug-loading capacity (DLC, %) of micelles were determined by high-performance liquid chromatography (HPLC, Waters). A standard curve was preconstructed by plotting peak area versus DTX concentrations ranging from 1 to 20 μg/mL (y = 30,168x − 14,520, R^2 = 0.9997). DTX was dissolved in methanol. HPLC conditions were as follows: C_{18} reversed-phase column; methanol/acetonitrile (35:65, v/v) as the mobile phase; and 230 nm as the detection wavelength. Afterward, 0.2 mL of freshly prepared micelle solution was treated with 3 mL of methanol, followed by sonication for 5 min. After filtering with a 0.22 μm filter, the solution containing loaded DTX was collected for HPLC analysis. Note that free DTX in water is ignorable, due to its poor water-solubility (<10 μg/mL experimentally). DLE is defined as loaded DTX relative to initially added DTX (w/w), and DLC is the DTX percentage in drug-loaded micelles. The weight of micelles was acquired after lyophilization. RhB loaded into micelles was treated with the same protocol and quantitatively analyzed based on a preconstructed standard curve (y = 133,633x − 49.067, 2−6 ng/mL, R^2 = 0.9991) on a fluorospectrophotometer (RF-5301 PC, Shimadzu). The excitation and emission wavelengths were 560 and 590 nm, respectively.

2.3.4. In Vitro Response to Hypoxia. Chemical hypoxia was generated using $Na_2S_2O_4$, according to our previous work.[25] Blank micelles were sealed in the hypoxic condition in a quartz cuvette for 12 h, and the changes in characteristic peaks of blank micelles before and after hypoxic treatment were recorded to study *in vitro* response to hypoxia on a UV−vis spectrophotometer (UV-2401PC, Shimadzu). Similarly, drug-loaded micelles were also sealed in the hypoxic condition, and at predetermined intervals, an equivalent solution was withdrawn and centrifuged to remove the released DTX

https://doi.org/10.1021/acsami.1c23737
ACS Appl. Mater. Interfaces 2022, 14, 20551−20565

aggregate. The residual containing unreleased DTX was then treated with methanol for HPLC analysis to study *in vitro* drug release triggered by hypoxia. A cumulative DTX release curve was acquired by plotting the percentage of the total released DTX at predetermined intervals relative to loaded DTX versus time.

2.4. Cell Experiments. *2.4.1. Cell Monolayer and Spheroid Culture.* 4T-1 and MDA-MB-231 cells were cultured in RPMI-1640 and L15 culture media, respectively, supplemented with 10% fetal bovine serum (FBS) and 1% antibiotics in a humidified CO_2 (5%) atmosphere. Cells growing as a monolayer were collected using trypsin, centrifuged, and then seeded at a density of 3000/well in a low attachment 384-well U-bottom plate (PrimeSurface, Sumilon) to form cell spheroids. The culture medium was refreshed every 1−2 days. Note that MDA-MB-231 cell spheroids were not formed using this plate.

2.4.2. Cellular Uptake, Tumor Penetration, and Hypoxia-Responsive Drug Release. The general cell monolayer treatment protocol: when growing to approximately 80% confluence under normoxia, 4T-1 or MDA-MB-231 cells were treated with RhB in its free form and loaded in micelles and subsequently incubated for 2 h under normoxia. After washing twice with phosphate-buffered saline (PBS) (pH = 7.4) to remove uninternalized RhB and micelles, the cells were subjected to normoxia, fixed hypoxia (1% O_2), and gradient hypoxia for another 3 h for further analysis. A hypoxia incubator (INVIVO2, Ruskinn) was used to generate the fixed hypoxia. The gradient hypoxia was generated by placing a φ14 mm coverslip onto the cells cultured and treated in a polystyrene/glass confocal dish (No. BDD011035, JET BIOFIL), where the oxygen concentration decreased from the edge to the center of the coverslip. The fluorescence from the cells was detected to study cellular uptake and hypoxia-responsive drug release on a confocal laser scanning microscope (CLSM, TCS SP8, Leica) using a RhB filter set.

Cell spheroids cultured in U-bottom wells for 7 days were treated to study tumor penetration and hypoxia-responsive drug release. Following the treatment under normoxia for 5 h, the spheroids were carefully washed with PBS (pH = 7.4), suctioned from wells, and put on a glass-bottom culture dish for fluorescence observation.

2.4.3. Cell Viability. 4T-1 and MDA-MB-231 monolayers and spheroids were treated with different DTX formulations, followed by washing with PBS (pH = 7.4), based on the protocol described in Section 2.4.2. Cell monolayers were further incubated under normoxia or hypoxia, for 48 and 6 h for the MTT assay and calcein-AM/PI double staining, respectively. Cell spheroids were incubated under normoxia for 24 h for calcein-AM/PI double staining. The MTT assay and calcein-AM/PI double staining were performed according to the standard protocol recommended by the manufacturer.

2.4.4. Cell Migration. Cell migration was assessed by wound healing. After the treatment according to the procedures described in Section 2.4.2, cell monolayers cultured in a 6-well plate were scratched using a 1 mL pipette to generate a wound area. After the incubation under normoxia and hypoxia, respectively, for 24 h, the wound of the cells was recorded on an inverted microscope. Cell migration ratio is defined as the reduced wound area after the treatment relative to the initial area without cells before the treatment. The wound area was acquired using ImageJ software.

2.5. Animal Experiments. *2.5.1. Tumor Model.* BALB/c mice were used to establish an orthotopic murine model of breast cancer metastasis. BALB/c mice were inoculated with a PBS suspension of 4T-1 cells (1×10^7 cells/mL, 100 μL) in the left 4th mammary fat pad. The mice were then housed in standard cages and given free access to food and water. The cell suspension was placed on ice prior to use.

2.5.2. Pharmacokinetics, Tissue Distribution, and NIR Imaging. A pharmacokinetic study was carried out in healthy BALB/c mice. The mice were intravenously injected with DTX in its free form and loaded in micelles at 10 mg/kg body weight. At predetermined intervals, the mice were euthanized and the blood sample taken from the mouse orbital was centrifuged at 8000 rpm for 10 min. The collected plasma was then treated with a mixed solution of chloroform and methanol (4:1, v/v) to extract DTX. Extracted DTX in the chloroform layer was collected after centrifugation at 8000 rpm for 10 min. After removing chloroform using a rotatory evaporator, the samples were added with methanol to completely precipitate the proteins. Following centrifugation, methanol solution containing DTX was collected and filtered for HPLC analysis.

Tissue distribution was assessed in tumor-bearing mice. When a tumor became palpable on the 14th day after tumor cell inoculation, the mice were intravenously injected with DTX in its free form and loaded in micelles at 10 mg/kg body weight. At 24 h post-injection, the mice were euthanized for perfusion-fixation and some main tissues, including the liver, spleen, lungs, kidneys, heart, and tumor, were then harvested. Tissue samples were homogenized in PBS (pH = 7.4) and treated to analyze DTX by the HPLC method using the procedure for pharmacokinetic studies.

In another experiment, tumor-bearing mice were intravenously injected with Cy5.5 loaded in micelles. At 24 h post-injection, the mice were euthanized and the tissues of the liver, spleen, lungs, heart, and tumor were harvested for NIR imaging using a small-animal dedicated IVIS imaging system (Lumina II, Caliper Life Sciences). Cy5.5 fluorescence intensity was acquired by IVIS imaging software.

2.5.3. Drug Treatment. On the 14th day after tumor cell inoculation, tumor-bearing mice were divided into six groups (five mice per group): (1) PBS control group; (2) free DTX (10 mg/kg); (3) DL-PMs/DTX (10 mg/kg); (4) SC-PMs/DTX (10 mg/kg); (5) AZO-SC-PMs/DTX (10 mg/kg); and (6) high-dose AZO-SC-PMs/DTX (20 mg/kg). Free DTX was dissolved in PBS containing DMSO (1%, v/v) for animal experiments as well as cell experiments. The mice intravenously received drug treatment every 4 days for a total of five times.

The body weight and tumor volume of the mice were monitored every other day, and the survival situation of the mice was checked every day. The tumor volume was calculated as $V = (L \times W^2)/2$, where L and W represent the tumor length and width, respectively. On the 31st day after tumor cell inoculation, all mice were euthanized and tumors were harvested from mice, weighed, and photographed. Moreover, tumors, as well as harvested lungs and livers, were rinsed with PBS (pH 7.4), fixed with paraformaldehyde, embedded in paraffin, and cut into slices for haematoxylin/eosin (H&E) staining. Lungs and livers were also fixed with Bouin's solution (Feiyu Bio, China) and photographed to observe metastatic nodules.

2.5.4. Safety Assessment. Before assessing therapeutic outcomes, hematologic and biochemical examinations were carried out to evaluate the drug tolerance of different drug formulations, which was also considered as a guide for the treatment dose. Healthy BALB/c mice received intravenous injection of PBS, DTX, DL-PMs/DTX, SC-PMs/DTX, and AZO-SC-PMs/DTX at 10 or 20 mg of DTX/kg every 4 days for a total of five times. At 24 h following the last injection, all mice were euthanized and blood samples were taken from the orbit. One part of each blood sample was used to count the white blood cells (WBCs), hemoglobin (HGB), and platelets (PLTs) on a BC-2800 Auto Hematology Analyzer (Mindray, China); the other was used to analyze aspartate aminotransferase (AST) and the total bilirubin on a clinically used biochemical analyzer (Roche).

In another experiment, after assessing therapeutic outcomes, other tissues of tumor-bearing mice, such as the heart, spleen, and kidneys, were harvested from the euthanized mice and prepared for H&E staining for histopathological examination.

2.6. Statistical Analysis. All data were analyzed using GraphPad Prism 8.0. Unpaired Student's *t*-test and the one-way analysis of variance (ANOVA) test were used to statistically compare two groups and multiple groups, respectively. A *p*-value below 0.05 ($p < 0.05$) was considered statistically significant.

3. RESULTS AND DISCUSSION

3.1. Stereocomplex Micelles Facilitate Drug Loading. We first synthesized a series of copolymers. To synthesize hypoxia-responsive copolymers, activated mPEG-NHS was used as the starting material, the NHS terminal of which was conjugated with AZO. The obtained mPEG-AZO was further

https://doi.org/10.1021/acsami.1c23737
ACS Appl. Mater. Interfaces 2022, 14, 20551−20565

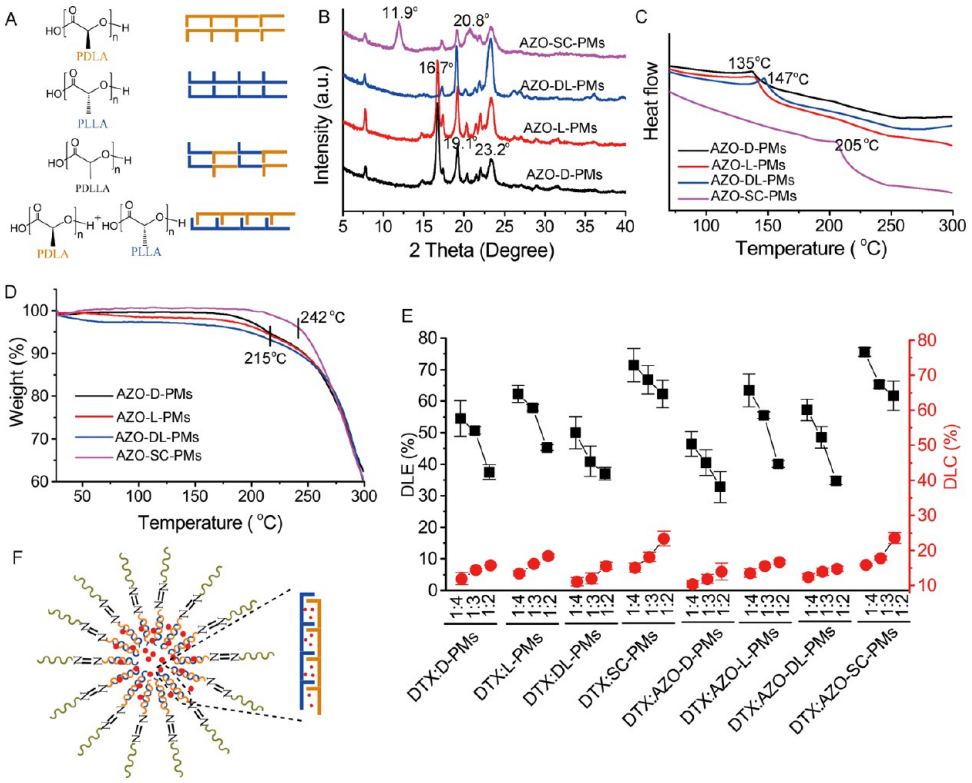

Figure 2. Stereocomplex structure with improved structural stability for drug loading. (A) Schematic illustration of stereocomplexation of PDLA and PLLA. (B) XRD, (C) DSC, and (D) TGA profiles of enantiomeric, racemic, and stereocomplex micelles. (E) DLE and DLC of enantiomeric, racemic, and stereocomplex micelles at varying DTX feeding. (F) Schematic illustration of high drug loading of stereocomplex micelles. Note that actual stereocomplexation should take place among many enantiomeric PDLA and PLLA molecules. Data are presented as mean ± standard deviation (SD) (n = 3).

conjugated with PDLA, PLLA, and PLA via a simple amide reaction, producing hypoxia-responsive mPEG-AZO-PDLA, mPEG-AZO-PLLA, and mPEG-AZO-PLA, respectively. AZO acted as a hypoxia-responsive linker of hydrophilic mPEG and hydrophobic PLA in these three copolymers. Nonresponsive mPEG-PDLA, mPEG-PLLA, and mPEG-PLA were also synthesized for comparison through a one-step amide reaction (Figure 1A,B). The successful synthesis of all copolymers was confirmed by ^{1}H NMR. As shown in Figure 1C,D, mPEG-PDLA, mPEG-PLLA, and mPEG-PLA show the peaks of mPEG at 3.4−3.7 ppm[28] and of PLA at 1.6 and 5.2 ppm,[29] while hypoxia-responsive copolymers display the characteristic peak of AZO at 7.8 ppm,[30] differentiating them from the nonresponsive ones. There was no difference among the three nonresponsive copolymers and among the three hypoxia-responsive copolymers.

Amphiphilic copolymers could self-assemble into micelles in aqueous conditions. CMC is the concentration above which micelles are formed. As the self-assembly of an amphiphilic copolymer is driven by its hydrophobic segment, stereocomplexation through tight packing of PLA segments is thus supposed to lower CMC of micelles. CMC values of AZO-D-PMs, AZO-L-PMs, AZO-DL-PMs, and AZO-SC-PMs were 26.3, 25.8, 22.5, and 10.1 mg/L, respectively. Stereocomplex micelles were of the lowest CMC as expected (Table S1). DLS further showed that all blank micelles possessed a hydrodynamic diameter (D_h) of 140−230 nm with a narrow size distribution (PDI < 0.25), and stereocomplex micelles (SC-PMs and AZO-SC-PMs) generally had a smaller D_h than enantiomeric (D-PMs, L-PMs, AZO-D-PMs, and AZO-L-PMs) and racemic micelles (DL-PMs and AZO-DL-PMs), also due to the tight packing of PLA segments. The AZO group led to a D_h increase of AZO-incorporated micelles in comparison to AZO-free micelles, as it reinforced the rigidity of copolymers as well as micelles.[31] All micelles were negatively charged with a ζ-potential less than −20 mV (Figure S1 and Table S1).

It has been reported that stereocomplex formation by blending equivalent enantiomeric PLA is driven by $CH_3\cdots O=C$, resulting in a new crystalline structure,[32] as illustrated in Figure 2A. Crystalline structures of AZO-D-PMs, AZO-L-PMs, AZO-DL-PMs, and AZO-SC-PMs were studied by their XRD patterns (Figure 2B). All micelles showed sharp peaks at 19.1 and 23.2°, belonging to the crystallized PEG segment.[33] A diffraction peak at 16.7°, reported for PLA homopolymers,[34] appeared in AZO-D-PMs and AZO-L-PMs, which disappeared in AZO-DL-PMs and AZO-SC-PMs. Especially, two new peaks appeared at 11.9 and 20.8° in AZO-SC-PMs, which were characteristic of the crystalline structure of stereocomplex PLA.[35] The XRD results indicated the formation of the stereocomplex structure and also confirmed the amorphous nature of racemic PLA.[36] Thermal properties of the micelles were determined by DSC and TGA. DSC profiles demonstrated that the melting temperature (T_m) of AZO-D-PMs and AZO-L-PMs was approximately 135 °C and it slightly increased to 147 °C for AZO-DL-PMs; after stereocomplexation, T_m increased by 70 °C, up to 205 °C (Figure 2C). TGA further showed that the thermal decomposition behavior of enantiomeric and racemic micelles was almost the same, and the rapid weight loss started from 215 °C in these samples;

https://doi.org/10.1021/acsami.1c23737
ACS Appl. Mater. Interfaces 2022, 14, 20551−20565

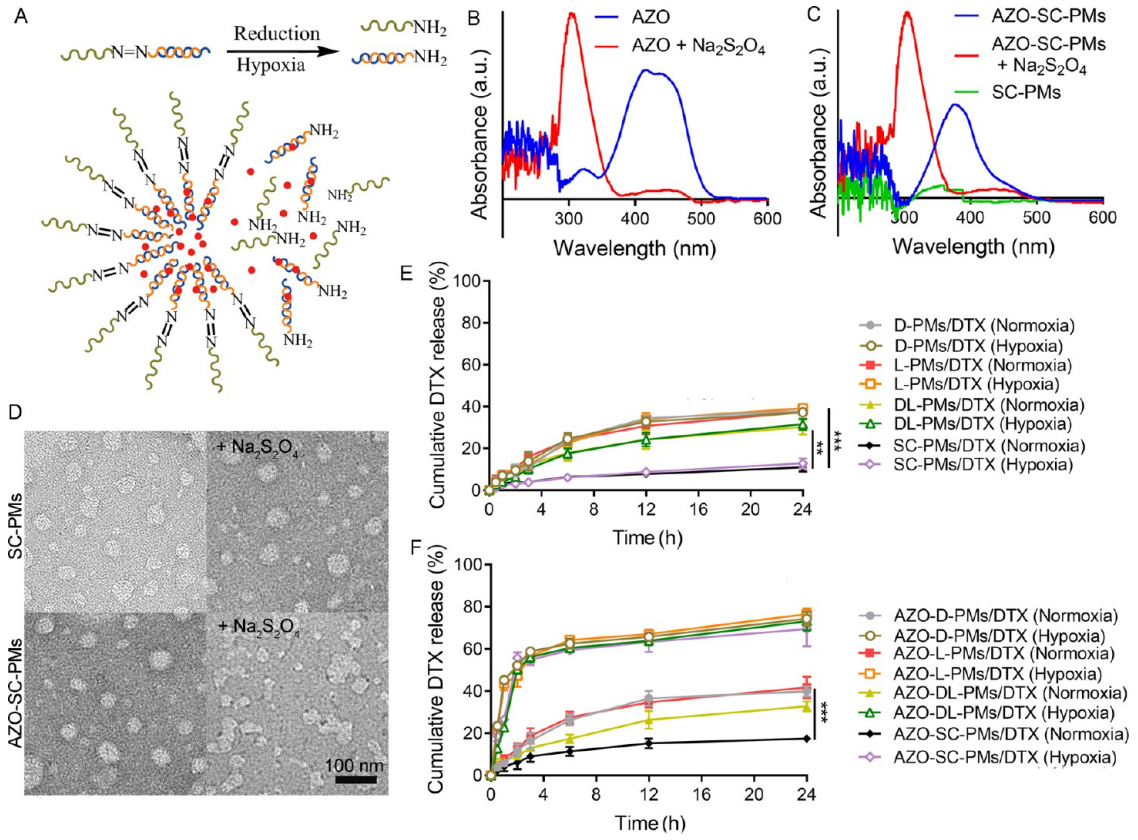

Figure 3. AZO cleavage in responding to hypoxia for the structural change of hypoxia-responsive micelles and concomitant drug release. (A) Schematic illustration of the response to hypoxia. UV−vis spectra of (B) AZO and (C) AZO-SC-PMs before and after hypoxic treatment. SC-PMs were considered as their corresponding controls. (D) TEM images of AZO-SC-PMs before and after hypoxic treatment with SC-PMs as a control. Cumulative drug release of (E) nonresponsive and (F) hypoxia-responsive enantiomeric, racemic, and stereocomplex micelles before and after hypoxic treatment. The hypoxic reductive condition was generated by $Na_2S_2O_4$. All data are presented as mean ± SD ($n = 3$). $^{**}p < 0.01$ SC-PMs versus DL-PMs and $^{***}p < 0.001$ SC-PMs versus D-PMs and L-PMs under normoxia in panel (E) and $^{***}p < 0.001$ AZO-SC-PMs versus AZO-D-PMs, AZO-L-PMs, and AZO-DL-PMs under normoxia in panel (F).

comparatively, the weight loss accelerated above 242 °C for stereocomplex micelles (Figure 2D). Stereocomplexation significantly improved the thermal properties of micelles for high structural stability. Thermal decomposition of all micelles with different configurations tended to be consistent when the temperature continued to rise, due to their same intrinsic nature.

As the stereocomplex structure endowed micelles with improved structural stability, its positive impact on drug loading and stability after drug loading was predictable. As shown in Figure 2E and Table S2, DLE values of AZO-D-PMs, AZO-L-PMs, and AZO-DL-PMs for an example of 1:4 of fed DTX to micelles were 46.4, 63.2, and 57.2% with 10.4, 13.6, and 12.5% in DLC, respectively; DLE and DLC increased to 75.6 and 15.9%, respectively, for AZO-SC-PMs. AZO-SC-PMs generally displayed a relatively high DLE and DLC in comparison to all other AZO-incorporated micelles. A similar phenomenon was found in AZO-free micelles. The stability of drug-loaded micelles was another concern. Micelle suspension with a massive precipitate was considered unstable. Drug loading had an insignificant effect on the D_h, PDI, and ζ-potential of the micelles (Table S3); however, it greatly affected the stability (Table S2). At 1:2 ratio of fed DTX to micelles, all drug-loaded micelles with a high DLC were unstable and a massive precipitate was observed within 0.5 h. With decreasing DTX feeding, the stability of all micelles increased and stereocomplex micelles, as well as racemic micelles, remained stable for more than 48 h, showing higher stability than enantiomeric micelles. It was interesting that AZO-L-PMs, as well as L-PMs, exhibited a higher loading capacity than their enantiomeric micelles and racemic micelles. Chirality in DTX for spatial interaction with PLLA might contribute to this result. Despite the high stability, the drug loading of racemic micelles was unsatisfactory. A high drug loading accompanied by high stability was achieved only in stereocomplex micelles, resulting from the entrapment of hydrophobic DTX in the stereocomplex PLA core with improved structural stability (Figure 2F). Note that in terms of drug loading and stability, DTX-loaded micelles at 1:4 ratio of fed DTX to micelles were used for all cell experiments as well as animal experiments at a dose of 10 mg/kg, while those at 1:3 ratio were used for animal experiments at a high dose of 20 mg/kg.

3.2. Hypoxia-Responsive Drug Release Augments *In Vitro* Antitumor Activity under Hypoxia. AZO, as a linker of hydrophilic and hydrophobic segments of the copolymers, will undergo reductive cleavage under hypoxia, leading to the structural change of self-assembled micelles and concomitant drug release (Figure 3A). UV−vis spectra revealed that free AZO displayed one broad peak around 414−440 nm and this peak shifted to 377 nm after being incorporated into micelles. Especially, the characteristic peak of AZO disappeared in all

https://doi.org/10.1021/acsami.1c23737
ACS Appl. Mater. Interfaces 2022, 14, 20551−20565

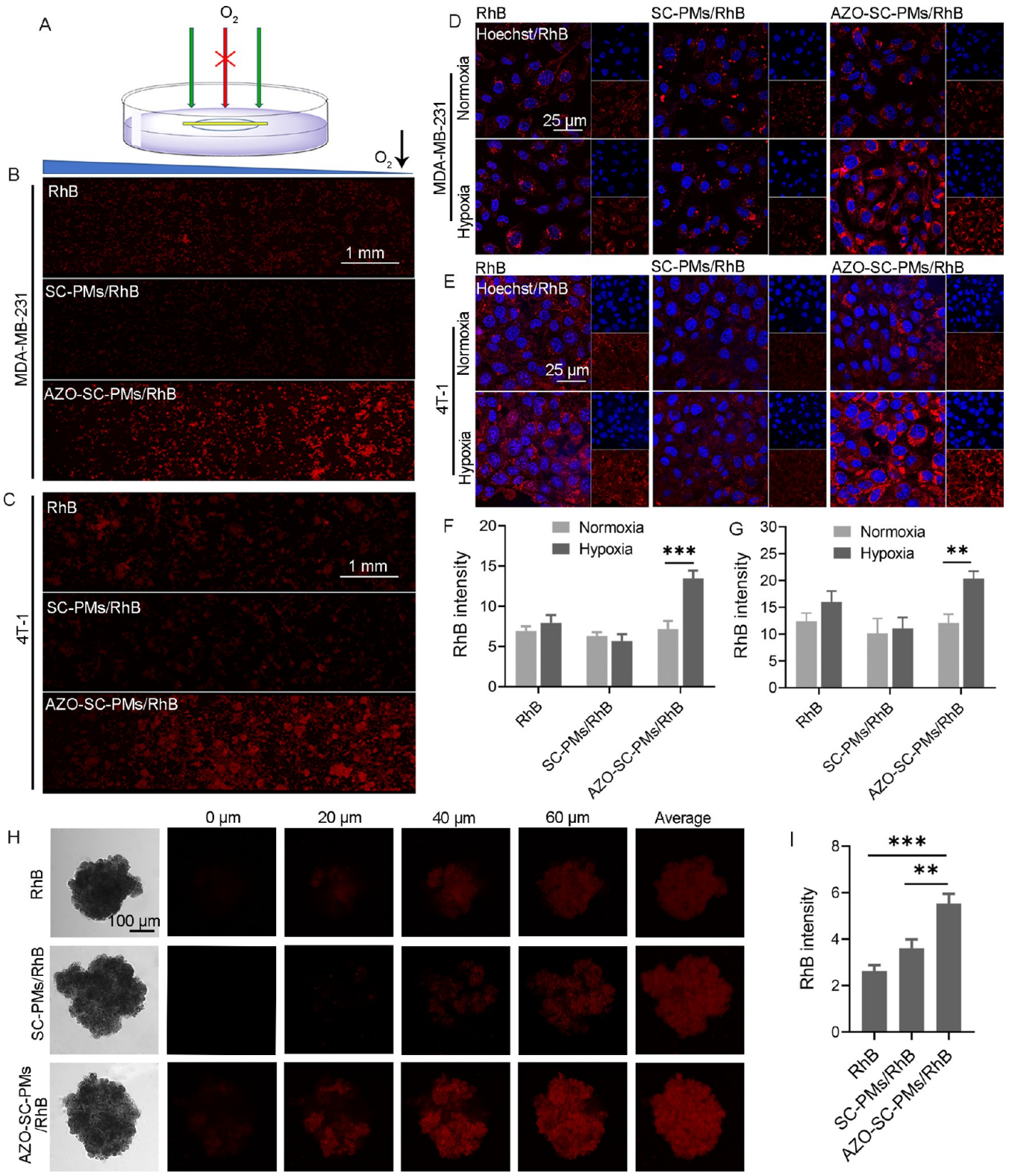

Figure 4. *In vitro* release in responding to hypoxic tumor cells. (A) Schematic illustration of the generation of gradient hypoxia by placing a coverslip onto the cells cultured and treated in a confocal dish. CLSM observation of RhB in (B) MDA-MB-231 and (C) 4T-1 cells under gradient hypoxia. CLSM observation of RhB in (D) MDA-MB-231 and (E) 4T-1 cells under a specific normoxia (21% O_2) and hypoxia (1% O_2) by a hypoxia workstation and (F and G) their corresponding quantitative analysis of RhB fluorescence. (H) CLSM observation of RhB in 4T-1 cell spheroids and (I) corresponding quantitative analysis of RhB fluorescence. All cells were treated with free RhB, SC-PMs/RhB, and AZO-SC-PMs/RhB with equivalent RhB. The data are acquired using ImageJ and presented as mean ± SD (n = 3). $^{**}p < 0.01$ and $^{***}p < 0.001$.

AZO-incorporated micelles, and a sharp peak belonging to the aniline group appeared at 306 nm when exposed to the reductive hypoxic condition generated by $Na_2S_2O_4$ (Figures 3B,C and S2). Nonresponsive SC-PMs displayed no character-

https://doi.org/10.1021/acsami.1c23737
ACS Appl. Mater. Interfaces 2022, 14, 20551−20565

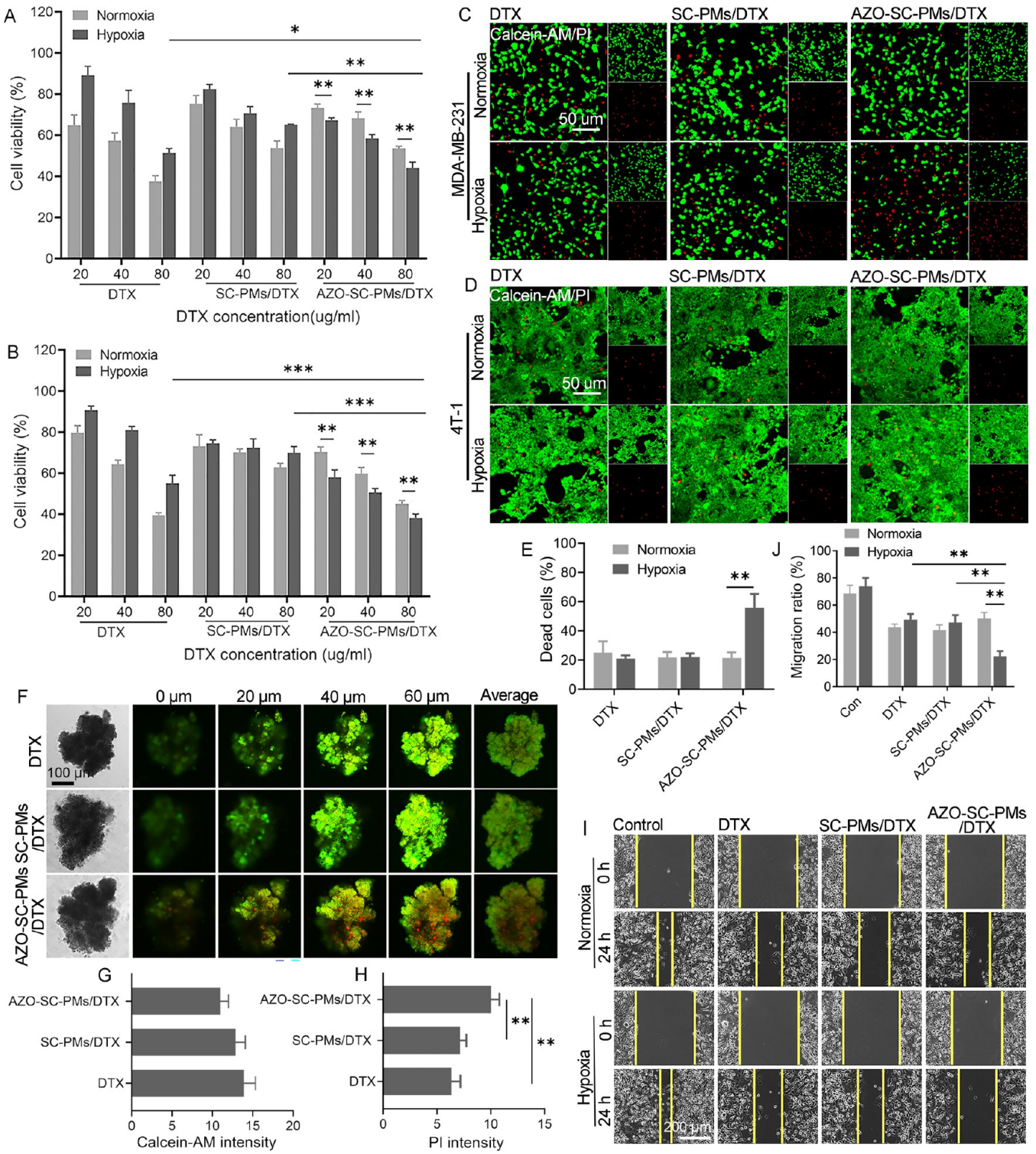

Figure 5. Hypoxia-responsive drug release for enhanced *in vitro* antitumor activity. The MTT assay of (A) MDA-MB-231 and (B) 4T-1 cells under normoxia and hypoxia. Calcein-AM/PI double staining of (C) MDA-MB-231 and (D) 4T-1 cells under normoxia and hypoxia and (E) quantitative analysis of MDA-MB-231 cells. (F) Calcein-AM/PI double staining of 4T-1 cell spheroids and the corresponding quantitative analysis of (G) calcein-AM and (H) PI fluorescence. (I) Wound-healing assay of 4T-1 cells under normoxia and hypoxia and (J) corresponding quantitative analysis of the migration ratio. The cells were treated with free DTX, SC-PMs/DTX, and AZO-SC-PMs/DTX with equivalent DTX. The DTX concentrations were 40, 140, and 20 μg/mL for panels (C) and (D), (F), and (I), respectively. Data are acquired using ImageJ and presented as mean ± SD (n = 6 for the MTT assay and n = 3 for the other experiments). *p < 0.05, **p < 0.01, and ***p < 0.001.

istic peaks. UV−vis spectra confirmed the cleavage of AZO after hypoxic treatment. The cleavage of AZO detached the hydrophilic and hydrophobic segments of the copolymers and thus destabilized the micelles. As validated by TEM images, SC-PMs could maintain their original size and spherical morphology, while AZO-SC-PMs seemed to fuse together and

https://doi.org/10.1021/acsami.1c23737
ACS Appl. Mater. Interfaces 2022, 14, 20551−20565

lost their original shape once exposed to hypoxia (Figure 3D). The diameters of both SC-PMs and AZO-SC-PMs in TEM were less than 100 nm, smaller than D_h. Cumulative release profiles demonstrated that all micelles gradually released their payloads under normoxia, and the premature drug release of SC-PMs was around 10% in 24 h, while it was more than 30% for D-PMs, L-PMs, and DL-PMs (Figure 3E). Stereocomplexation significantly improved the stability of the micelles (**p < 0.01 SC-PMs versus DL-PMs and ***p < 0.001 SC-PMs versus D-PMs and L-PMs under normoxia). AZO-incorporated stereocomplex micelles also displayed a higher stability under normoxia (***p < 0.001 AZO-SC-PMs versus AZO-D-PMs, AZO-L-PMs, and AZO-DL-PMs), although AZO incorporation partially impaired their stability, as characterized by increased premature drug leakage (Figure 3F). Importantly, AZO-free micelles remained stable under hypoxia, showing the same release behavior as those under normoxia; in contrast, the drug release of AZO-incorporated micelles was remarkably accelerated under hypoxia, almost approaching a plateau within 3 h, as a result of the hypoxia-triggered structural change. AZO-SC-PMs thus possessed a high stability under physiological conditions and a high sensitivity for drug release in responding to hypoxia.

Cell experiments were performed to study the cellular uptake and tumor penetration of the micelles for enhanced *in vitro* antitumor activity in responding to hypoxia. We first placed a coverslip onto the cells in a confocal dish, resulting in gradient hypoxia with the oxygen supply gradually decreasing from the edge to the center of the coverslip (Figure 4A). CLSM images exhibited that the fluorescence intensity from the cells treated with RhB and SC-PMs/RhB remained consistent under gradient hypoxia. Comparatively, the fluorescence intensity from the AZO-SC-PMs/RhB group increased along with a decreased oxygen supply (Figure 4B,C), indicating the high sensitivity in responding to hypoxia. In the following, the hypoxia workstation was used to study hypoxia-responsive release under specific hypoxia (1% O_2). Different from RhB and SC-PMs/RhB groups showing no difference in the fluorescence intensity under normoxia (21% O_2) and hypoxia, the AZO-SC-PMs/RhB group exhibited a significantly higher intensity under hypoxia than under normoxia (Figure 4D−G). CLSM results also demonstrated that internalized RhB in its free form and loaded in micelles was mainly located in the cytoplasm, unable to enter the nucleus. A similar trend was found in MDA-MB-231 and 4T-1 cells. The hypoxia-responsive release was further evaluated in tumor cell spheroids that could better mimic actual tumor microenvironments. Tumor cell spheroids were observed by CLSM z-stack scanning from the top with a spheroid surface defined as 0 μm. As shown in Figure 4H,I, AZO-SC-PMs/RhB penetrated the whole spheroids and displayed a significantly high average fluorescence intensity, as a result of spontaneously responding to the hypoxic environment of cell spheroids.

Generally, the fluorescence intensity of the AZO-SC-PMs/RhB group under hypoxia is significantly higher than that of the free RhB group, solidly corroborating that nanocarriers enhance cellular uptake through nanoparticle-mediated endocytosis. The inconformity that compared with RhB, SC-PMs/RhB display a weak fluorescence in cell monolayers, due to the shield effect of micelles, but a strong fluorescence in cell spheroids, indicates that nanocarriers greatly facilitate tumor penetration for cellular uptake. In addition, as emphasized in Section 2.4.2, the cell monolayers were treated with different RhB formulations and allowed for uptake for 3 h, followed by the removal of uninternalized formulations before hypoxic treatment. Therefore, hypoxia-responsive release takes place inside cells at least, in this case, indicating that hypoxia promotes the overexpression of some intracellular reductases including azoreductase to reduce AZO for drug release.[37] The overexpressed azoreductase is reported to be localized in the lysosome, in recent work.[38] Moreover, as the only stimulus exerted to cells to trigger release is hypoxia, regardless of tumor cell types, it strongly suggests that the hypoxia-responsive drug delivery system is reliable and universal.

The therapeutic outcome of a drug formulation is highly associated with its effective drug dose. As responsive drug release considerably improves the local drug dose, enhanced *in vitro* antitumor activity of AZO-SC-PMs/DTX under hypoxia is predictable. *In vitro* antitumor activity was first determined by the MTT assay. All drug formulations exhibited concentration-dependent cytotoxicity against MDA-MB-231 and 4T-1 cells (Figure 5A,B). DTX showed limited cytotoxicity under hypoxia, due to hypoxia-induced resistance to chemotherapy.[39] Although improved cellular uptake was achieved, the SC-PMs/DTX group still presented an unsatisfactory therapeutic outcome under hypoxia, which was even suppressed at high drug concentrations compared with free DTX. Endowing SC-PMs/DTX with a responsive feature augmented the antitumor activity of micelles. AZO-SC-PMs/DTX presented a significantly increased cytotoxicity under hypoxia, showing a statistical difference in comparison to free DTX and SC-PMs/DTX. The trend in MDA-MD-231 and 4T-1 cells was the same. The micelles without drug loading were nontoxic to the cells, regardless of normoxia or hypoxia (Figure S3). Calcein-AM/PI double staining was carried out to detect living/dead cells. It was observed that dead cells in the AZO-SC-PMs/DTX group increased under hypoxia, as compared to DTX and SC-PMs/DTX groups (Figures 5C,D and S4). Quantitative analysis further demonstrated that more than 50% of MDA-MB-231 cells were dead in the AZO-SC-PMs/DTX group under hypoxia, whereas cell death was not more than 30% in all other groups (Figure 5E). AZO-SC-PMs/DTX significantly aggravated cell death under hypoxia. Noting that due to the growth in the cluster, it was difficult to quantitatively analyze the dead ratio of 4T-1 cells. Calcein-AM/PI double staining was also performed in cell spheroids. The results demonstrated that as compared to DTX and SC-PMs/DTX groups, calcein-AM fluorescence decreased, while the PI fluorescence increased in the AZO-SC-PMs/DTX group (Figure 5F). Quantitative analysis further confirmed that although no significant difference in the calcein-AM fluorescence intensity was observed, the PI fluorescence intensity in the AZO-SC-PMs/DTX group was significantly higher than those in DTX and SC-PMs/DTX groups (Figure 5G,H), as a result of facilitated tumor penetration for hypoxia-responsive release. Cell migration is an important step for distant metastasis of tumor cells. As a nonexpensive and highly reproducible method, the wound-healing assay was executed to determine the inhibitory effect of AZO-SC-PMs/DTX on tumor cell migration under hypoxia. The results demonstrated that hypoxia generally promoted cell migration in DTX and SC-PMs/DTX groups as well as in the control group. This result was well consistent with that in the MTT assay, where cell viability was augmented under hypoxia. AZO-SC-PMs/DTX reversed hypoxia-promoted cell migration, showing a considerable inhibitory effect (Figure 5I,J).

https://doi.org/10.1021/acsami.1c23737
ACS Appl. Mater. Interfaces 2022, 14, 20551−20565

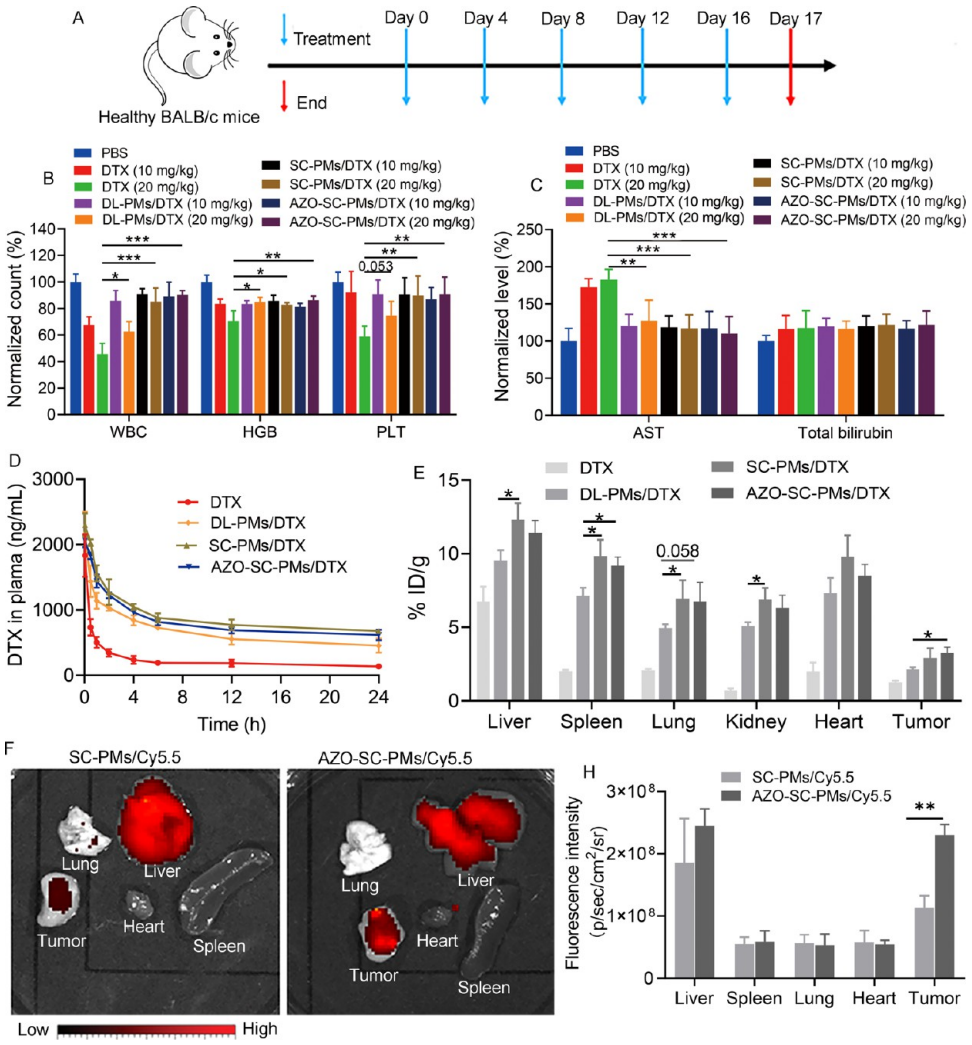

Figure 6. Drug tolerance evaluation and improved tissue distribution of hypoxia-responsive stereocomplex micelles for triggered release in responding to intratumoral hypoxia. (A) Protocol of drug treatment for hematologic and biochemical examinations. (B) Normalized count of WBCs, HGB, and PLTs at 24 h following the last treatment. (C) Normalized level of AST and total bilirubin at 24 h following the last treatment. Healthy BALB/c mice received intravenous injection of PBS, DTX, DL-PMs/DTX, SC-PMs/DTX, and AZO-SC-PMs/DTX at 10 or 20 mg of DTX/kg body weight every 4 days for a total of five times. (D) DTX content in plasma over time. Healthy BALB/c mice received intravenous injection of PBS, DTX, DL-PMs/DTX, SC-PMs/DTX, and AZO-SC-PMs/DTX at 10 mg of DTX/kg body weight. (E) DTX content in the liver, spleen, lungs, kidneys, heart, and tumor at 24 h post-injection. Tumor-bearing mice received intravenous injection of DTX, DL-PMs/DTX, SC-PMs/DTX, and AZO-SC-PMs/DTX at 10 mg of DTX/kg body weight. ID/g = injected dose per gram tissue. (E) NIR fluorescence imaging of harvested tissues at 24 h post-injection and (F) corresponding quantitative analysis. Data were acquired by IVIS software. (G) Tumor-bearing mice received intravenous injection of SC-PMs/Cy5.5 and AZO-SC-PMs/Cy5.5. Data are presented as mean ± SD (n = 4−5 for hematologic and biochemical examinations and n = 3 for the other experiments). *p < 0.05, **p < 0.01, and ***p < 0.001.

Together, these results corroborate the fact that hypoxia promotes cell proliferation and migration for metastasis and induces drug resistance, thus setting a major obstacle to chemotherapy. Although it has been widely reported that nanoparticles as drug carriers are capable of attenuating the resistance of tumor cells to chemotherapy through a series of mechanisms,[40] *in vitro* antitumor activity of SC-PMs/DTX is still inhibited, due to their high stability that makes effective drug dose remain low. It thus recommends that a drug delivery system with very high stability is not an optimal choice for cancer therapy. Of course, the high stability of a carrier is beneficial to biocompatibility, as SC-PMs/DTX with improved cellular uptake is less toxic than free DTX. Once endowed with a hypoxia-responsive moiety, AZO-SC-PMs/DTX reverse hypoxia-induced drug resistance and hypoxia-promoted cell migration. The augmented antitumor activity of AZO-SC-PMs/DTX is achieved by facilitated tumor penetration and cellular uptake mediated by nanoparticles for rapid drug release to an effective drug dose in responding to hypoxia.

3.3. Stereocomplex Micelles Facilitate Drug Accumulation for Hypoxia-Responsive Intratumoral Release. Hematologic and biochemical examinations were first carried out to evaluate the systemic toxicity of different drug formulations and guide treatment doses using the protocol illustrated in Figure 6A. Hematologic examination revealed that drug treatment generally decreased WBCs, HGB, and PLTs, especially exhibiting a dose-dependent decrease in the DTX group (Figure 6B). The DL-PMs/DTX group exhibited a higher drug tolerance than the DTX group, and the increased DL-PMs/DTX dose lowered WBC and PLT but had no considerable effect on HGB. Importantly, hematology functions in SC-PMs/DTX and AZO-SC-PMs/DTX remained

https://doi.org/10.1021/acsami.1c23737
ACS Appl. Mater. Interfaces 2022, 14, 20551−20565

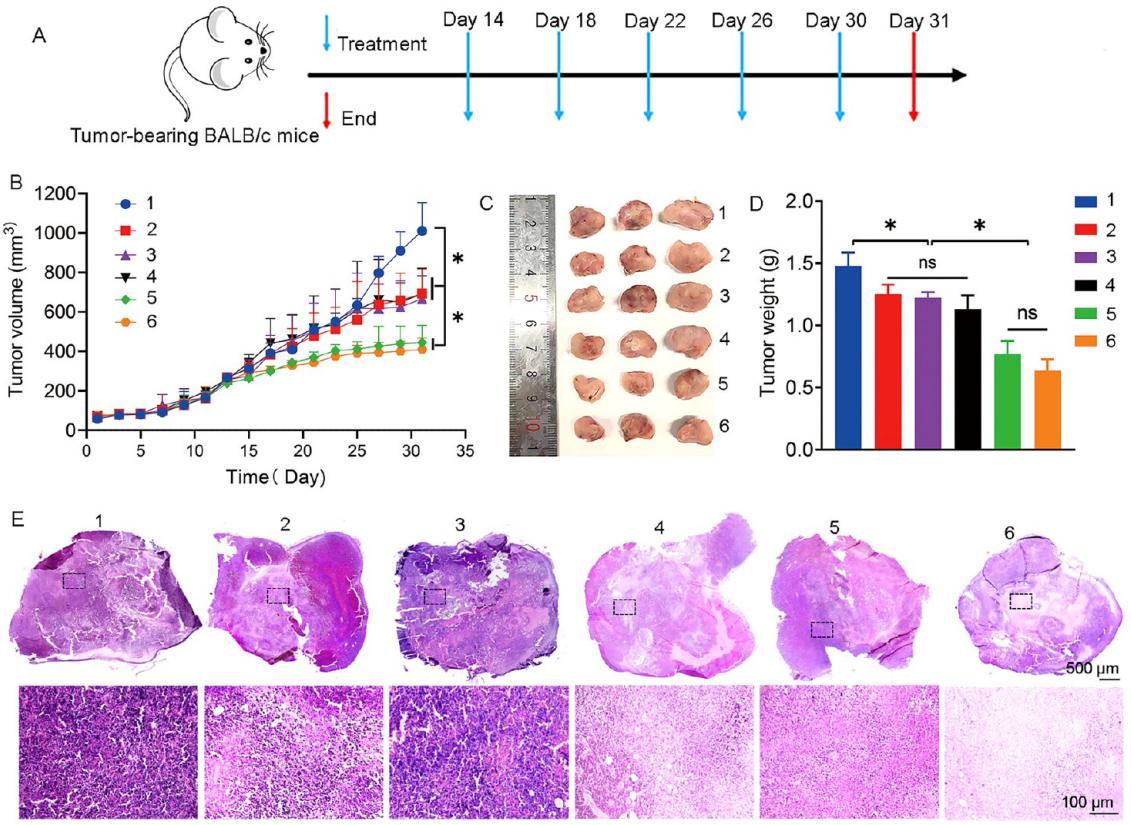

Figure 7. *In vivo* therapeutic outcome in inhibiting the growth of the primary 4T-1 tumor. (A) Protocol of drug treatment for *in vivo* antitumor activity evaluation. (B) Tumor volume monitoring over time. (C) Digital images of harvested tumors and (D) tumor weight at the end of the experimental period. (E) H&E staining images of the whole tumor section and the corresponding zoomed images. Starting from the 14th day, BALB/c mice received intravenous injection of PBS, DTX, DL-PMs/DTX, SC-PMs/DTX, and AZO-SC-PMs/DTX at 10 or 20 mg of DTX/kg body weight every 4 days for a total of five times. Data are presented as mean ± SD (n = 3−6). *p < 0.05. 1 = PBS, 2 = DTX (10 mg/kg), 3 = DL-PMs/DTX (10 mg/kg), 4 = SC-PMs/DTX (10 mg/kg), 5 = AZO-SC-PMs/DTX (10 mg/kg), and 6 = high-dose AZO-SC-PMs/DTX (20 mg/kg).

relatively high, regardless of the drug dose. Biochemical examination further revealed that DTX treatment led to the increase of AST reflecting the liver function and encapsulating DTX into micelles reduced its damage to the liver (Figure 6C). No significant change was observed in total bilirubin after drug treatment. Based on hematologic and biochemical examinations, 10 mg of DTX/kg is considered a relatively safe dose for all drug formulations, while 20 mg of DTX/kg is safe only for stereocomplex micelles. The improved drug tolerance of stereocomplex micelles is attributed to the high stability of the stereocomplex structure that prevented micelles from premature leakage for prolonged blood circulation time, as evidenced by the pharmacokinetic study (Figure 6D).

The 4T-1 cell line, derived from a spontaneous BALB/c mammary tumor, is one of the highly metastatic cancer cell lines. The 4T-1 tumor can spontaneously metastasize mainly to the lungs and second to the liver through blood and/or lymphatic routes, while the primary tumor still grows in situ, resembling human metastatic breast cancer.[41,42] 4T-1 cells were thus injected into the mammary fat pad of BALB/c mice to establish an orthotopic murine model of breast cancer metastasis. The accumulation of a drug, especially in tumors, is a vital characteristic to determine its therapeutic outcome. Tissue distribution was carried out to assess the effect of the stereocomplex structure on drug accumulation in various tissues including tumors. As shown in Figure S5, all drug formulations were widely distributed to the liver, spleen, lungs, kidneys, heart, and tumor at 12 h post-injection; DTX-loaded micelles exhibited a high tissue accumulation in comparison to free DTX, indicating that DTX experienced a different metabolism route when encapsulated into micelles. Tissue accumulation of DTX-loaded micelles, as well as DTX in normal tissues, decreased over time while increasing in tumors, due to the enhanced permeation and retention (EPR) effects (Figure 6E). Moreover, it was observed that SC-PMs/DTX generally had a higher tissue accumulation than DL-PMs/DTX. One reason is that SC-PMs/DTX is more stable than DL-PMs/DTX for a prolonged blood circulation time and improved pharmacokinetic performance (Figure 6D and Table S4), favoring their distribution to various tissues. Another possible reason is that since SC-PMs/DTX has a higher drug loading with more DTX in one micelle, according to Figure 2E, more DTX is taken up when phagocytosis of tissues reaches a saturation point. Figure 6E also revealed a reduced accumulation of AZO-SC-PMs/DTX in normal tissues, due to stability impairment caused by rigid AZO. Especially, the accumulation of SC-PMs/DTX, as well as AZO-SC-PMs/DTX, in tumors was found to be higher than that of DL-PMs/DTX. It therefore strongly suggests that nanoparticles with a high drug loading can facilitate drug accumulation in tumors for enhanced therapeutic outcomes.

As the HPLC method, used to quantitatively determine the DTX content in tumors, was unable to differentiate released DTX from encapsulated DTX, NIR imaging was performed to

https://doi.org/10.1021/acsami.1c23737
ACS Appl. Mater. Interfaces 2022, 14, 20551−20565

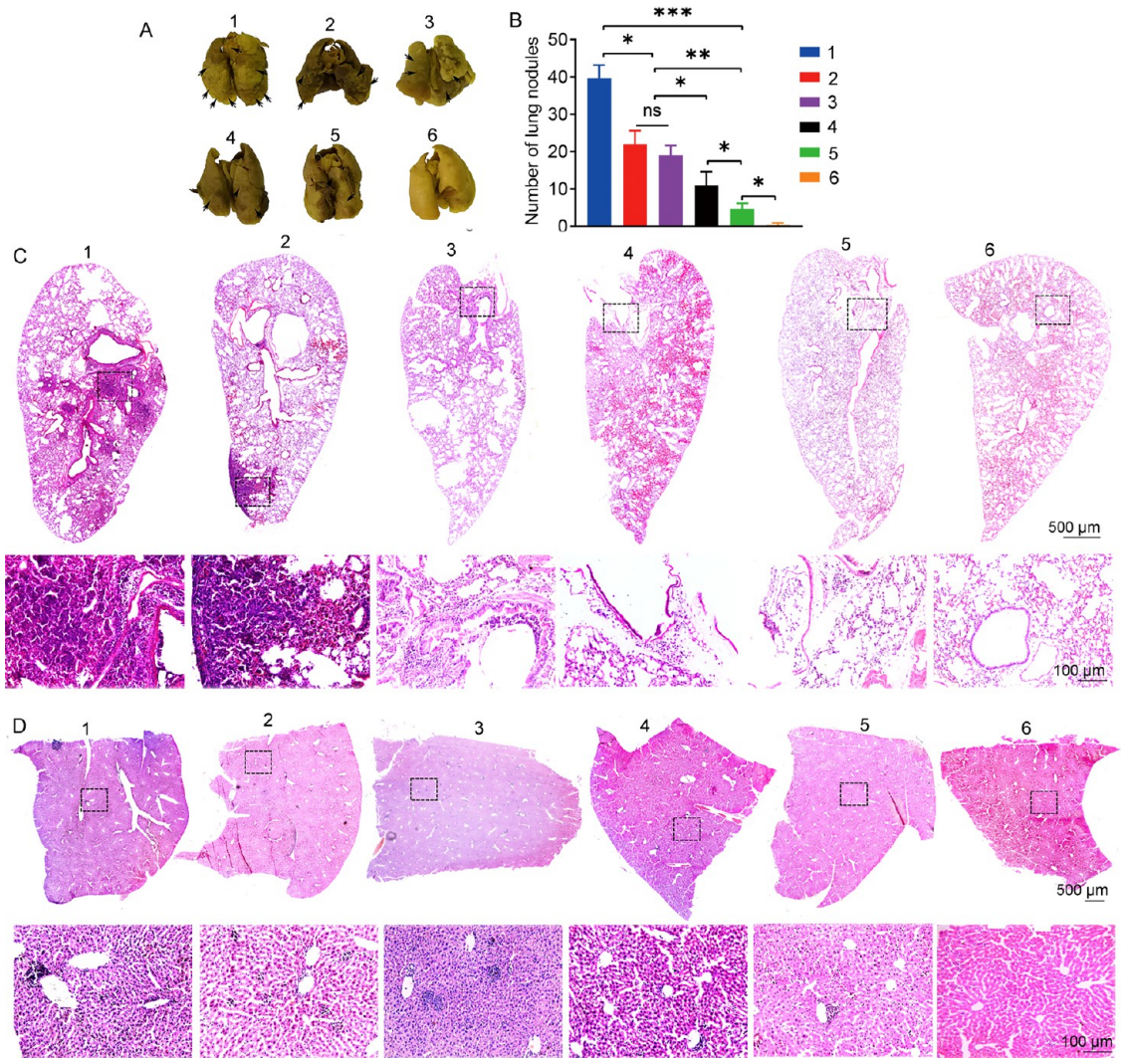

Figure 8. *In vivo* therapeutic outcomes in inhibiting 4T-1 tumor metastasis to the lungs and liver. (A) Digital images of harvested lungs after Bouin's fixation and (B) number of macroscopic metastatic nodules on the surface of lungs. Black arrows indicate metastatic nodules. H&E staining images of the whole (C) lungs and (D) liver section and the corresponding zoomed images. Starting from the 14th day, BALB/c mice received intravenous injection of PBS, DTX, DL-PMs/DTX, SC-PMs/DTX, and AZO-SC-PMs/DTX at 10 or 20 mg of DTX/kg body weight every 4 days for a total of five times. Data are presented as mean ± SD (n = 3−6). *p < 0.05, **p < 0.01, and ***p < 0.001. 1 = PBS, 2 = DTX (10 mg/kg), 3 = DL-PMs/DTX (10 mg/kg), 4 = SC-PMs/DTX (10 mg/kg), 5 = AZO-SC-PMs/DTX (10 mg/kg), and 6 = high-dose AZO-SC-PMs/DTX (20 mg/kg).

evaluate hypoxia-responsive intratumoral release. Tumor-bearing mice received intravenous injection of SC-PMs/Cy5.5 and AZO-SC-PMs/Cy5.5, and at 24 h post-injection, some main tissues were imaged. As shown in Figure 6F,H, AZO-SC-PMs/Cy5.5 exhibited an approximate fluorescence intensity in normal tissues but a significantly high fluorescence intensity in tumors, as compared to SC-PMs/Cy5.5. According to drug tissue distribution, SC-PMs/Cy5.5 and AZO-SC-PMs/Cy5.5 should be of approximate accumulation in tumors. The significantly high fluorescence intensity of AZO-SC-PMs/Cy5.5 in tumors was thus attributed to the triggered release in responding to intratumoral hypoxia. It is worth noting that drug accumulation of DTX-loaded micelles in the kidneys was comparable to that in the spleen, lungs, and heart, whereas the fluorescence intensity of Cy5.5-loaded micelles in the kidneys was outstandingly high, covering the fluorescence in tumors (Figure S6). Different metabolic routes of DTX and Cy5.5 might lead to this huge difference. As NIR imaging is mainly used to observe hypoxia-responsive release in tumors, the NIR image of the kidneys is not provided herein. No metastatic nodules were observed in the lungs as well as other normal tissues at this experimental point.

3.4. Hypoxia-Responsive Stereocomplex Micelles Inhibit the Growth and Metastasis of Orthotopic Breast Cancer. To evaluate the therapeutic outcome of different drug formulations, tumor-bearing mice intravenously received treatment of PBS, DTX, DL-PMs/DTX, SC-PMs/DTX, and AZO-SC-PMs/DTX at 10 mg of DTX/kg every 4 days for a total of five times, which started from the 14th day after tumor cell inoculation (Figure 7A). A high-dose group (20 mg of DTX/kg for AZO-SC-PMs/DTX) was additionally performed. Figure 7B demonstrated that the tumor volume in the PBS group gradually increased over time. After treatment, tumor growth in DTX, DL-PMs/DTX, and SC-PMs/DTX was inhibited (*p < 0.01 versus PBS); however, no difference was found among these three groups. Parallel *in vivo* antitumor

https://doi.org/10.1021/acsami.1c23737
ACS Appl. Mater. Interfaces 2022, 14, 20551−20565

activity of DL-PMs/DTX with free DTX was also observed in the literature,[14] despite improved drug accumulation in the tumor through the EPR effects. This result was in good coincidence with the clinical data that the outstanding advantage of Nanoxel M using DL-PMs as carriers over DTX is MTD but not antitumor activity.[43] It was noted that although SC-PMs/DTX did not exhibit superior therapeutic outcomes in inhibited tumor growth over DL-PMs/DTX, they were capable of alleviating histological conditions of tumors and effectively inhibiting tumor metastasis, as discussed later. AZO-SC-PMs/DTX remarkably augmented therapeutic outcomes, showing a significant difference in inhibiting tumor growth relative to the other groups ($*p < 0.05$ versus DTX, DL-PMs/DTX, and SC-PMs/DTX). It thus implies that a rapid drug release to an effective dose in tumors is crucial for nanocarrier-based chemotherapy. At the end of the experimental period, the tumors were harvested, photographed, and weighed. As shown in Figure 7C, tumor sizes in the two AZO-SC-PMs/DTX groups were visibly smaller than those in the other groups. The tumor weight accorded well with the tumor size (Figure 7D). Histological characteristics of the tumors in different groups were evaluated by H&E staining. Figure 7E provides H&E staining images of the whole tumor tissue section and the corresponding zoomed images. It was observed that tumor cells in the PBS group packed tightly and were filled with abundant stroma, indicating that tumor cells were in rapid proliferation. DTX, as well as DL-PMs/DTX, showed a certain antitumor efficacy, and the proliferation of tumor cells was inhibited with a little scattered necrotic area observed in these two groups. SC-PMs/DTX considerably alleviated histological manifestation of tumors with condensed nuclei and a large necrotic area, contrasting starkly with the result in Figure 7B that SC-PMs/DTX showed no difference in inhibiting tumor growth, as compared to DTX and DL-PMs/DTX. AZO-SC-PMs/DTX exhibited satisfactory therapeutic outcomes with few tumor cells and larger necrotic areas, especially in the high-dose group, which was attributed to hypoxia-responsive release after drug accumulation. During the experimental period, drug treatment did not significantly prolong survival time; however, it delayed the death of the mice (Figure S7A). Especially, the number of dead mice in the AZO-SC-PMs/DTX group was found to be less than that in the other groups. Drug treatment had no effect on the body weight of the mice (Figure S7B). No body weight loss was found in all groups, suggesting that the micelles even at a high drug dose were not toxic, which was consistent with hematologic and biochemical examinations. Moreover, the mice in the PBS group were observed to be emaciated along with aggravated tumor burden. An emaciated body and increased tumor size balanced the body weight, making it not different from the other groups.

The capability of the micelles in inhibiting tumor metastasis to distant organs, such as the lungs and liver, was our concern. Harvested lungs and livers were fixed with Bouin's solution and photographed. As demonstrated in Figure 8A,B, breast cancer aggressively metastasized to the lungs, showing a great number of macroscopic metastatic nodules on the surface of the lungs in the PBS group. After treatment with DTX and DL-PMs/DTX, tumor metastasis was inhibited with reduced metastatic nodules ($*p < 0.05$ versus PBS). No significant difference was observed in these two groups. Less metastatic nodules were observed in the SC-PMs/DTX group ($*p < 0.05$ versus DTX and DL-PMs/DTX), probably due to alleviated histological manifestation of tumors and/or improved drug accumulation in the lungs. AZO-SC-PMs/DTX further inhibited tumor metastasis to the lungs, showing a significant difference in comparison to the other groups. ($*p < 0.05$ versus SC-PMs/DTX, $**p < 0.01$ versus DTX and DL-PMs/DTX, and $***p < 0.001$ versus PBS). Especially, the high-dose AZO-SC-PMs/DTX group showed a remarkable efficacy in inhibiting tumor metastasis and almost no metastatic nodules were observed. No metastatic nodules were observed on the surface of the livers in all groups (Figure S8). Histological characteristics of the lungs and livers were also evaluated by H&E staining. As shown in Figure 8C, the PBS group was characteristic of a damaged pulmonary architecture accompanied by large metastatic foci, irregular pulmonary bronchioles, and thickened alveolar walls, displaying pathological evidence of lung metastasis.[44] These pathological characteristics were still observed after treatment with DTX and DL-PMs/DTX, and pulmonary architecture damage seemed to be alleviated in some extent after treatment with SC-PMs/DTX. Tumor metastasis to the lungs was considerably inhibited after treatment with AZO-SC-PMs/DTX, with only some little metastatic foci observed. Especially, the pulmonary architecture was well preserved in the high-dose AZO-SC-PMs/DTX group, appearing normal with uniformly expanded alveoli throughout the lungs and normal pulmonary vessels and alveolar walls.[45] On the other hand, although there were no macroscopic metastatic nodules on the surface of the livers in all groups, H&E staining revealed that histological change occurred, which was characterized by the formation of a lot of metastatic foci around hepatic vessels (Figure 8D). The number of metastatic foci was reduced after treatment with AZO-SC-PMs/DTX and notably, metastatic foci were barely observed in the high-dose AZO-SC-PMs/DTX group. H&E staining of the lungs and liver verified the high efficacy of AZO-SC-PMs/DTX, especially at a high dose, in inhibiting breast cancer metastasis to distant organs, although their efficacy in inhibiting primary tumor growth was not eye-catching. Moreover, although there was no difference in the tumor volume among DTX, DL-PMs/DTX, and SC-PMs/DTX, pathological conditions in the tumor, lungs, and liver in the SC-PMs/DTX group were better than those in DTX and DL-PMs/DTX groups. Generally, the high efficacy of AZO-SC-PMs/DTX in inhibiting breast cancer metastasis to the lungs and liver is owing to the following factors: (1) the stereocomplex structure of AZO-SC-PMs/DTX facilitates drug delivery to tumors for hypoxia-triggered release, which greatly maximizes bioavailability of DTX to effectively kill tumor cells and inhibit their distant metastasis and (2) the stereocomplex structure of the micelles facilitates drug delivery to the lungs as well as the other tissues, which also effectively kill metastatic tumor cells.

At the end of the whole experiment, some other tissues including the heart, kidneys, and spleen were also harvested for H&E staining (Figure S9). No infiltration of the 4T-1 tumor to these tissues was observed in all groups. Drug treatment also did not cause remarkable tissue toxicity.

CONCLUSIONS

In summary, we attempted to fabricate hypoxia-responsive stereocomplex PEG-PLA micelles to treat breast cancer metastasis. We first synthesized a series of copolymers for the self-assembly of enantiomeric, racemic, and stereocomplex micelles. Stereocomplex micelles showed high structural stability, improving drug loading and reducing drug leakage.

https://doi.org/10.1021/acsami.1c23737
ACS Appl. Mater. Interfaces 2022, 14, 20551−20565

Once endowed with a hypoxia-responsive feature, the micelles were capable of sensitively responding to the hypoxic tumor microenvironment, leading to enhanced bioavailability under hypoxia. *In vivo* results further showed that the micelles, especially at a high dose, inhibited the growth of the primary tumor and remarkably inhibited its metastasis to the lungs and liver, as a result of effective drug delivery, facilitated by the stereocomplex structure, and the subsequent hypoxia-responsive drug release at hypoxic sites. Together with high biocompatibility, hypoxia-responsive stereocomplex micelles were therefore a safe and effective drug delivery system in treating breast cancer metastasis.

■ ASSOCIATED CONTENT

Supporting Information

The Supporting Information is available free of charge at https://pubs.acs.org/doi/10.1021/acsami.1c23737.

Detailed synthetic procedures of copolymers; CMC, D_h, ζ-potential, drug loading, and stability of micelles; MTT assay and calcein-AM/PI double staining of MDA-MB-231 and 4T-1 cells; pharmacokinetics; drug tissue distribution; NIR imaging; and H&E staining (PDF)

■ AUTHOR INFORMATION

Corresponding Authors

Li Zhu − *Institute of Special Environmental Medicine and Co-innovation Center of Neuroregeneration, Nantong University, Nantong 226019, People's Republic of China*; Email: Zhulizhou@ntu.edu.cn

Qianqian Luo − *Institute of Special Environmental Medicine and Co-innovation Center of Neuroregeneration, Nantong University, Nantong 226019, People's Republic of China*; Email: qianqianluo@ntu.edu.cn

Zhongping Chen − *Institute of Special Environmental Medicine and Co-innovation Center of Neuroregeneration, Nantong University, Nantong 226019, People's Republic of China*; orcid.org/0000-0002-3344-1449; Phone: +86513-55003378; Email: chenzp@ntu.edu.cn

Authors

Min Lu − *Institute of Special Environmental Medicine and Co-innovation Center of Neuroregeneration, Nantong University, Nantong 226019, People's Republic of China*

Xu Huang − *Institute of Special Environmental Medicine and Co-innovation Center of Neuroregeneration, Nantong University, Nantong 226019, People's Republic of China*

Xiaohui Cai − *Department of Hematology, Nanjing Medical University, Affiliated Changzhou No. 2 People's Hospital, Changzhou 213000, People's Republic of China*

Jiajia Sun − *Institute of Special Environmental Medicine and Co-innovation Center of Neuroregeneration, Nantong University, Nantong 226019, People's Republic of China*

Xuemeng Liu − *Institute of Special Environmental Medicine and Co-innovation Center of Neuroregeneration, Nantong University, Nantong 226019, People's Republic of China*

Lingyan Weng − *Institute of Special Environmental Medicine and Co-innovation Center of Neuroregeneration, Nantong University, Nantong 226019, People's Republic of China*

Complete contact information is available at: https://pubs.acs.org/10.1021/acsami.1c23737

Author Contributions

[§]M.L. and X.H. contributed equally to this work. The manuscript was written through contributions of all authors. All authors have given approval to the final version of the manuscript.

Notes

The authors declare no competing financial interest.

■ ACKNOWLEDGMENTS

The work was supported by the National Natural Science Foundation of China (81401506, 81971131, and 81873924) and the Science and Technology Project of Changzhou Health Committee (CJ20210068).

■ REFERENCES

(1) Siegel, R. L.; Miller, K. D.; Jemal, A. Cancer Statistics 2020. *Ca-Cancer J. Clin.* **2020**, *70*, 7−30.

(2) Fang, X.; Cao, J.; Shen, A. Advances in Anti-Breast Cancer Drugs and the Application of Nano-Drug Delivery Systems in Breast Cancer Therapy. *J. Drug Delivery Sci. Technol.* **2020**, *57*, No. 101662.

(3) Gong, C.; Yu, X.; You, B.; Wu, Y.; Wang, R.; Han, L.; Wang, Y.; Gao, S.; Yuan, Y. Macrophage-Cancer Hybrid Membrane-Coated Nanoparticles for Targeting Lung Metastasis in Breast Cancer Therapy. *J. Nanobiotechnol.* **2020**, *18*, No. 92.

(4) Hwang, D.; Ramsey, J. D.; Kabanov, A. V. Polymeric Micelles for the Delivery of Poorly Soluble Drugs: From Nanoformulation to Clinical Approval. *Adv. Drug Delivery Rev.* **2020**, *156*, 80−118.

(5) Wang, J.; Li, S.; Han, Y.; Guan, J.; Chung, S.; Wang, C.; Li, D. Poly(Ethylene Glycol)-Polylactide Micelles for Cancer Therapy. *Front. Pharmacol.* **2018**, *9*, No. 202.

(6) Zheng, X.; Xie, J.; Zhang, X.; Sun, W.; Zhao, H.; Li, Y.; Wang, C. An Overview of Polymeric Nanomicelles in Clinical Trials and on the Market. *Chin. Chem. Lett.* **2021**, *32*, 243−257.

(7) Fraguas-Sánchez, A. I.; Martín-Sabroso, C.; Fernández-Carballido, A.; Torres-Suárez, A. I. Current Status of Nanomedicine in the Chemotherapy of Breast Cancer. *Cancer Chemother. Pharmacol.* **2019**, *84*, 689−706.

(8) Lee, S. W.; Yun, M. H.; Jeong, S. W.; In, C. H.; Kim, J. Y.; Seo, M. H.; Pai, C. M.; Kim, S. O. Development of Docetaxel-Loaded Intravenous Formulation, Nanoxel-Pm (T_m) Using Polymer-Based Delivery System. *J. Controlled Release* **2011**, *155*, 262−271.

(9) Werner, M. E.; Cummings, N. D.; Sethi, M.; Wang, E. C.; Sukumar, R.; Moore, D. T.; Wang, A. Z. Preclinical Evaluation of Genexol-Pm, a Nanoparticle Formulation of Paclitaxel, as a Novel Radiosensitizer for the Treatment of Non-Small Cell Lung Cancer. *Int. J. Radiat. Oncol., Biol., Phys.* **2013**, *86*, 463−468.

(10) Ding, J. X.; Chen, L. H.; Xiao, C. S.; Chen, L.; Zhuang, X. L.; Chen, X. S. Noncovalent Interaction-Assisted Polymeric Micelles for Controlled Drug Delivery. *Chem. Commun.* **2014**, *50*, 11274−11290.

(11) Li, Z. B.; Tan, B. H.; Lin, T. T.; He, C. B. Recent Advances in Stereocomplexation of Enantiomeric Pla-Based Copolymers and Applications. *Prog. Polym. Sci.* **2016**, *62*, 22−72.

(12) Liu, Y.; Xu, C.; Fan, X.; Loh, X. J.; Wu, Y.-L.; Li, Z. Preparation of Mixed Micelles Carrying Folates and Stable Radicals through Pla Stereocomplexation for Drug Delivery. *Mater. Sci. Eng., C* **2020**, *108*, No. 110464.

(13) Luo, F.; Fortenberry, A.; Ren, J.; Qiang, Z. Recent Progress in Enhancing Poly(Lactic Acid) Stereocomplex Formation for Material Property Improvement. *Front. Chem.* **2020**, *8*, No. 688.

(14) Tam, Y. T.; Shin, D. H.; Chen, K. E.; Kwon, G. S. Poly(Ethylene Glycol)-Block-Poly(D,L-Lactic Acid) Micelles Containing Oligo(Lactic Acid)8-Paclitaxel Prodrug: In Vivo Conversion and Antitumor Efficacy. *J. Controlled Release* **2019**, *298*, 186−193.

(15) Tam, Y. T.; Huang, C.; Poellmann, M.; Kwon, G. S. Stereocomplex Prodrugs of Oligo(Lactic Acid)N-Gemcitabine in Poly(Ethylene Glycol)-Block-Poly(D,L-Lactic Acid) Micelles for

Improved Physical Stability and Enhanced Antitumor Efficacy. *ACS Nano* **2018**, *12*, 7406−7414.
(16) Wang, H.; Zhou, L.; Xie, K.; Wu, J.; Song, P.; Xie, H.; Zhou, L.; Liu, J.; Xu, X.; Shen, Y.; Zheng, S. Polylactide-Tethered Prodrugs in Polymeric Nanoparticles as Reliable Nanomedicines for the Efficient Eradication of Patient-Derived Hepatocellular Carcinoma. *Theranostics* **2018**, *8*, 3949−3963.
(17) Repp, L.; Rasoulianboroujeni, M.; Lee, H. J.; Kwon, G. S. Acyl and Oligo(Lactic Acid) Prodrugs for Peg-B-Pla and Peg-B-Pcl Nano-Assemblies for Injection. *J. Controlled Release* **2021**, *330*, 1004−1015.
(18) Long, M. M.; Lu, A. L.; Lu, M.; Weng, L. Y.; Chen, Q. P.; Zhu, L.; Chen, Z. P. Azo-Inserted Responsive Hybrid Liposomes for Hypoxia-Specific Drug Delivery. *Acta Biomater.* **2020**, *115*, 343−357.
(19) Zhou, Q.; Zhang, L.; Yang, T.; Wu, H. Stimuli-Responsive Polymeric Micelles for Drug Delivery and Cancer Therapy. *Int. J. Nanomed.* **2018**, *13*, 2921−2942.
(20) Kumari, R.; Sunil, D.; Ningthoujam, R. S. Hypoxia-Responsive Nanoparticle Based Drug Delivery Systems in Cancer Therapy: An up-to-Date Review. *J. Controlled Release* **2020**, *319*, 135−156.
(21) Mi, P. Stimuli-Responsive Nanocarriers for Drug Delivery, Tumor Imaging, Therapy and Theranostics. *Theranostics* **2020**, *10*, 4557−4588.
(22) Li, Y.; Jeon, J.; Park, J. H. Hypoxia-Responsive Nanoparticles for Tumor-Targeted Drug Delivery. *Cancer Lett.* **2020**, *490*, 31−43.
(23) Li, Y.; Lu, A. L.; Long, M. M.; Cui, L.; Chen, Z. P.; Zhu, L. Nitroimidazole Derivative Incorporated Liposomes for Hypoxia-Triggered Drug Delivery and Enhanced Therapeutic Efficacy in Patient-Derived Tumor Xenografts. *Acta Biomater.* **2019**, *83*, 334−348.
(24) Liu, X. M.; Luo, Q. Q.; Chen, Z. P. Co-Delivery of Chloroquine and Doxorubicin by Hypoxia-Responsive Liposomes for Enhanced Synergistic Antitumor Activity in Treating Solid Tumor. *Nanosci. Nanotechnol. Lett.* **2020**, *12*, 1309−1314.
(25) Long, M. M.; Liu, X. M.; Huang, X. L.; Lu, M.; Wu, X. M.; Weng, L. Y.; Chen, Q. P.; Wang, X. T.; Zhu, L.; Chen, Z. P. Alendronate-Functionalized Hypoxia-Responsive Polymeric Micelles for Targeted Therapy of Bone Metastatic Prostate Cancer. *J. Controlled Release* **2021**, *334*, 303−317.
(26) Lu, A.; Wang, J.; Najarro, M. C.; Li, S.; Deratani, A. Synthesis and Self-Assembly of Ab2-Type Amphiphilic Copolymers from Biobased Hydroxypropyl Methyl Cellulose and Poly(L-Lactide). *Carbohydr. Polym.* **2019**, *211*, 133−140.
(27) Muller, J.; Marchandeau, F.; Prelot, B.; Zajac, J.; Robin, J.-J.; Monge, S. Self-Organization in Water of Well-Defined Amphiphilic Poly(Vinyl Acetate)-B-Poly(Vinyl Alcohol) Diblock Copolymers. *Polym. Chem.* **2015**, *6*, 3063−3073.
(28) Masud; Kim, K. M.; Kim, H. K. Polymer Gel Electrolytes Based on Peg-Functionalized Aba Triblock Copolymers for Quasi-Solid-State Dye-Sensitized Solar Cells: Molecular Engineering and Key Factors. *ACS Appl. Mater. Interfaces* **2020**, *12*, 42067−42080.
(29) Oz, Y.; Nabawy, A.; Fedeli, S.; Gupta, A.; Huang, R.; Sanyal, A.; Rotello, V. M. Biodegradable Poly(Lactic Acid) Stabilized Nano-emulsions for the Treatment of Multidrug-Resistant Bacterial Biofilms. *ACS Appl. Mater. Interfaces* **2021**, *13*, 40325−40331.
(30) Zhou, P.-K.; Zong, L.-L.; Song, K.-Y.; Yang, Z.-C.; Li, H.-H.; Chen, Z.-R. Embedding Azobenzol-Decorated Tetraphenylethylene into the Polymer Matrix to Implement a Ternary Memory Device with High Working Temperature/Humidity. *ACS Appl. Mater. Interfaces* **2021**, *13*, 50350−50357.
(31) Butler, C. S. G.; King, J. P.; Giles, L. W.; Marlow, J. B.; Vidallon, M. L. P.; Sokolova, A.; de Campo, L.; Tuck, K. L.; Tabor, R. F. Design and Synthesis of an Azobenzene−Betaine Surfactant for Photo-Rheological Fluids. *J. Colloid Interface Sci.* **2021**, *594*, 669−680.
(32) Tam, Y. T. *Oligo (Lactic Acid)[N] Prodrugs for Poly(Ethylene Glycol)-Block-Poly(D,L-Lactic Acid) Micelles in Drug Delivery*; University of Wisconsin: Madison, 2018.
(33) Li, S.; Vert, M. Synthesis, Characterization, and Stereocomplex-Induced Gelation of Block Copolymers Prepared by Ring-Opening Polymerization of L(D)-Lactide in the Presence of Poly(Ethylene Glycol). *Macromolecules* **2003**, *36*, 8008−8014.
(34) Li, R. L.; Wu, Y. F.; Bai, Z. Y.; Guo, J. B.; Chen, X. L. Effect of Molecular Weight of Polyethylene Glycol on Crystallization Behaviors, Thermal Properties and Tensile Performance of Polylactic Acid Stereocomplexes. *RSC Adv.* **2020**, *10*, 42120−42127.
(35) Feng, C.; Piao, M.; Li, D. Stereocomplex-Reinforced Pegylated Polylactide Micelle for Optimized Drug Delivery. *Polymers* **2016**, *8*, No. 165.
(36) Kang, N.; Perron, M. E.; Prud'homme, R. E.; Zhang, Y. B.; Gaucher, G.; Leroux, J. C. Stereocomplex Block Copolymer Micelles: Core-Shell Nanostructures with Enhanced Stability. *Nano Lett.* **2005**, *5*, 315−319.
(37) Kumari, R.; Sunil, D.; Ningthoujam, R. S. Naphthalimides in Fluorescent Imaging of Tumor Hypoxia—an up-to-Date Review. *Bioorg. Chem.* **2019**, *88*, No. 102979.
(38) Zhu, C.; Zou, Z.; Huang, C.; Zheng, J.; Liu, N.; Li, J.; Yang, R. Highly Selective Imaging of Lysosomal Azoreductase under Hypoxia Using Ph-Regulated and Target-Activated Fluorescent Nanoprobes. *Chem. Commun.* **2019**, *55*, 3235−3238.
(39) Yang, J.; Li, W.; Luo, L. H.; Jiang, M. S.; Zhu, C. Q.; Qin, B.; Yin, H.; Yuan, X. L.; Yin, X. Y.; Zhang, J. L.; Luo, Z. Y.; Du, Y. Z.; You, J. Hypoxic Tumor Therapy by Hemoglobin-Mediated Drug Delivery and Reversal of Hypoxia-Induced Chemoresistance. *Biomaterials* **2018**, *182*, 145−156.
(40) Yao, Y.; Zhou, Y.; Liu, L.; Xu, Y.; Chen, Q.; Wang, Y.; Wu, S.; Deng, Y.; Zhang, J.; Shao, A. Nanoparticle-Based Drug Delivery in Cancer Therapy and Its Role in Overcoming Drug Resistance. *Front. Mol. Biosci.* **2020**, *7*, 193.
(41) Gao, Z.-G.; Tian, L.; Hu, J.; Park, I.-S.; Bae, Y. H. Prevention of Metastasis in a 4t1 Murine Breast Cancer Model by Doxorubicin Carried by Folate Conjugated Ph Sensitive Polymeric Micelles. *J. Controlled Release* **2011**, *152*, 84−89.
(42) Sun, Y.; Liu, L.; Zhou, L.; Yu, S.; Lan, Y.; Liang, Q.; Liu, J.; Cao, A.; Liu, Y. Tumor Microenvironment-Triggered Charge Reversal Polymetformin-Based Nanosystem Co-Delivered Doxorubicin and Il-12 Cytokine Gene for Chemo−Gene Combination Therapy on Metastatic Breast Cancer. *ACS Appl. Mater. Interfaces* **2020**, *12*, 45873−45890.
(43) Logie, J.; Ganesh, A. N.; Aman, A. M.; Al-awar, R. S.; Shoichet, M. S. Preclinical Evaluation of Taxane-Binding Peptide-Modified Polymeric Micelles Loaded with Docetaxel in an Orthotopic Breast Cancer Mouse Model. *Biomaterials* **2017**, *123*, 39−47.
(44) Benipal, B.; Feinstein, S. I.; Chatterjee, S.; Dodia, C.; Fisher, A. B. Inhibition of the Phospholipase A2 Activity of Peroxiredoxin 6 Prevents Lung Damage with Exposure to Hyperoxia. *Redox Biol.* **2015**, *4*, 321−327.
(45) Mendoza, A.; Hong, S.-H.; Osborne, T.; Khan, M. A.; Campbell, K.; Briggs, J.; Eleswarapu, A.; Buquo, L.; Ren, L.; Hewitt, S. M.; Dakir, E.-H.; Garfield, S.; Walker, R.; Merlino, G.; Green, J. E.; Hunter, K. W.; Wakefield, L. M.; Khanna, C. Modeling Metastasis Biology and Therapy in Real Time in the Mouse Lung. *J. Clin. Invest.* **2010**, *120*, 2979−2988.

https://doi.org/10.1021/acsami.1c23737
ACS Appl. Mater. Interfaces 2022, 14, 20551−20565